Broadband optical scattering in coupled silicon nanocylinders

C. Wang, Z. Y. Jia, K. Zhang, Y. Zhou, R. H. Fan, X. Xiong, and R. W. Peng[a)]
National Laboratory of Solid State Microstructures and Department of Physics, National Center of Microstructures and Quantum Manipulation, Nanjing University, Nanjing 210093, China

In this work, we demonstrate the broadband scattering of light waves incident on coupled silicon nanocylinders. First, it is shown that both electric and magnetic resonances are observed in a single silicon nanocylinder. By using two silicon nanocylinders, we next construct a silicon nanodimer. Thereafter, the original electric and magnetic resonances of the single nanocylinder shift and form hybrid resonant modes in the dimer; meanwhile, a new magnetic resonant mode emerges at a longer wavelength. Consequently, the silicon nanodimer exhibits a broadband scattering response that originates from optically magnetic interactions between dimeric silicon nanocylinders. Furthermore, the scattering bandwidth further increases upon using a silicon nanotrimer. This broadband optical response in silicon nanocylinders is demonstrated via their scattering spectra, and the magnetic interaction is verified by examining the spatial distributions of electromagnetic fields and the retrieved permittivity and permeability of the nanocylinders system. This theoretical finding may provide an approach to realize silicon-based broadband nanoantennas and nanosensors. © 2014 AIP Publishing LLC. [http://dx.doi.org/10.1063/1.4885766]

I. INTRODUCTION

With the development of microtechnology and nanotechnology, the ability to manipulate light at nanoscale levels is critical for future optical on-chip integration. However, due to the diffraction limit, conventional optical elements need to be redesigned for the subwavelength scale. Plasmonic nanoantennas, which are known for their ability to concentrate light to subwavelength volumes,[1–3] are considered a promising solution to the above problem. Inspired by the microwave antenna, different types of nanoantennas such as nanoapertures antenna array,[4] nanorod, bowtie,[5] Yagi-Uda nanoantenna,[6,7] and cross optical antenna[8] have been investigated. However, plasmonic nanoantennas, which are generally fabricated using noble metals such as Ag or Au, suffer from intrinsic losses at optical frequencies. This drawback affects their possible practical use in subwavelength optical sensors and detectors and so on. Fortunately, recent experimental demonstration of similar resonant properties achieved using high-refractive index dielectric nanoparticles[9,10] provides an alternative approach. These dielectric nanoparticles avoid the limitation of losses in metals (as in plasmonic nanoantennas) while exhibiting resonant properties similar to those of metallic particles. These research works are expected to pave the way toward the realization of low-loss optical devices such as all-dielectric or hybrid metal-dielectric nanoantennas.[11–14]

In contrast to metallic nanoparticles, for which the resonant scattering is dominated by electric resonances (dipole or quadrupole), high-index dielectric nanoparticles exhibit both electric and magnetic resonances at visible and infrared regimes.[15–19] The optical magnetic resonance originates

from the excited circular displacement current of the electric field inside the dielectric nanoparticle. Though metallic split-ring resonators[20] and multilayered metal/dielectric nanostructures[21] have obtained magnetic optical resonance via a circular current, high-index dielectric nanoparticles are advantageous in terms of easy fabrication and reduced cost. Further, high-index dielectric nanoparticles such as silicon can be easily integrated with existing semiconductor devices, thereby exhibiting potential usage in a wide range of comprehensive applications in future optical on-chip integration.

However, thus far, most studies have focused on single high-index dielectric nanoparticle[17,19,22–24] or periodic arrays[16,25,26] whose unit cells are still single nanoparticle. Very recently, the interactions between high-index dielectric nanoparticles have been explored.[26–31] When adjacent nanoparticles interact with each other, they can exhibit hybridized, particular modes. These hybridized modes can be involved in achieving some interesting features such as Fano resonances[27,28] or electric and magnetic field enhancement.[29,30] In the light of examining the properties of multiple high-index nanoparticles, we have theoretically investigated the behavior of resonances in dimeric and trimeric silicon nanocylinders in this work. We believe that this work will contribute to the development of dielectric nanoantennas from those based on single-particle systems to multi-particle antenna systems, thereby offering a unique avenue for future practical use in solar cells, nanosensors, and nanodetectors.

In this work, we numerically investigate the scattering properties of silicon nanocylinders by using finite-difference time-domain (FDTD)[32] simulation. In comparison with the single nanocylinder, the use of dimer and trimer introduces an additional dimension (gap size) for improving the performance of dielectric optical devices through the coupling between silicon nanocylinders in close proximity. Upon

---

[a)]Author to whom correspondence should be addressed. Electronic mail: rwpeng@nju.edu.cn

varying the gap size between the individual constituent nano-cylinders, the interparticle interaction can range from weak to strong. Accompanying the intense interaction, a new magnetic resonant mode which can be attributed to magnetic-to-magnetic interactions between the constituent nanocylinders emerges in dimeric or trimeric nanocylinders, exhibiting broadband scattering characteristics in contrast with single one. Furthermore, by introducing more complex interactions, trimeric silicon nanocylinders exhibit a more obvious bandwidth increase as expected. The broadband response in dielectric nanostructures can effectively be implemented to

design broadband dielectric nanoantennas and in other applications such as solar cells.

II. THEORETICAL MODEL AND ANALYSIS

According to the electric and magnetic resonant characteristics of dielectric nanoparticles, first we give the electromagnetic radiation of the electric and magnetic dipoles. The fields $\vec{E}_p$ and $\vec{H}_p$ at the location with a spatial distance of r and unit vector of direction $\vec{n}$ from an electric dipole, $\vec{p}$, can be expressed as

$$\begin{cases} \vec{E}_p = \dfrac{1}{4\pi\varepsilon_0}\left[\vec{p}\dfrac{e^{ikr}}{r}\left(k^2 - \dfrac{1}{r^2} + \dfrac{ik}{r}\right) + \vec{n}(\vec{n}\cdot\vec{p})\dfrac{e^{ikr}}{r}\left(-k^2 + \dfrac{3}{r^2} - \dfrac{3ik}{r}\right)\right] \\ \vec{H}_p = \dfrac{1}{4\pi(\mu_0\varepsilon_0)^{1/2}}\left[(\vec{n}\times\vec{p})\dfrac{e^{ikr}}{r}\left(k^2 + \dfrac{ik}{r}\right)\right], \end{cases} \tag{1}$$

where ε_0 and μ_0 denote the electric permittivity and magnetic permeability of vacuum, respectively, and k the wavevector of vacuum. The corresponding fields $\vec{E}_m$ and $\vec{H}_m$ from a magnetic dipole, $\vec{m}$, are given as

$$\begin{cases} \vec{E}_m = -\dfrac{1}{4\pi}\left(\dfrac{\mu_0}{\varepsilon_0}\right)^{1/2}(\vec{n}\times\vec{m})\dfrac{e^{ikr}}{r}\left(k^2 + \dfrac{ik}{r}\right) \\ \vec{H}_m = \dfrac{1}{4\pi}\left[\vec{m}\dfrac{e^{ikr}}{r}\left(k^2 - \dfrac{1}{r^2} + \dfrac{ik}{r}\right) + \vec{n}(\vec{n}\cdot\vec{m})e^{ikr}\left(-k^2 + \dfrac{3}{r^2} - \dfrac{3ik}{r}\right)\right]. \end{cases} \tag{2}$$

In the long-wavelength limit, when the characteristic size of the silicon nanoparticle is considerably smaller than the incident wavelength, the resulting optical resonances can be described by the effective electric and magnetic dipoles as below:

$$\vec{p} = \varepsilon_0\alpha_E\vec{E}_0, \quad \vec{m} = \chi_H\vec{H}_0, \tag{3}$$

where $\vec{p}$ and $\vec{m}$ denote the induced electric and magnetic dipoles, respectively, α_E and χ_H the electric and magnetic polarizabilities, respectively, and $\vec{E}_0$ and $\vec{H}_0$ the incident fields.

To consider the interaction between silicon nanoparticles, we introduce the coupled electric and magnetic dipole method proposed by Mulholland *et al.*[33] In our system, each particle is regarded as a composition of two dipoles, one electric and the other magnetic. Consequently, the electric and magnetic fields at the *ith* particle induced by the *jth* particle can be written as

$$\begin{cases} \vec{E}_i = a_{ij}\alpha_E\vec{E}_j + b_{ij}\alpha_E(\vec{E}_j\cdot\vec{n}_{ji})\vec{n}_{ji} - d_{ij}\left(\dfrac{\mu_0}{\varepsilon_0}\right)^{1/2}\chi_H(\vec{n}_{ji}\times\vec{H}_j) \\ \vec{H}_i = a_{ij}\chi_H\vec{H}_j + b_{ij}\chi_H(\vec{H}_j\cdot\vec{n}_{ji})\vec{n}_{ji} + d_{ij}\left(\dfrac{\varepsilon_0}{\mu_0}\right)^{1/2}\alpha_E(\vec{n}_{ji}\times\vec{E}_j), \end{cases} \tag{4}$$

where $\vec{n}_{ji}$ denote the direction vector from the *jth* particle to *ith* particle. The shorthand coefficients a_{ij}, b_{ij}, and d_{ij} from Eqs. (1) and (2) are expressed as

$$\begin{cases} a_{ij} = \dfrac{1}{4\pi}\dfrac{e^{ikr_{ij}}}{r_{ij}}\left(k^2 - \dfrac{1}{r_{ij}^2} + \dfrac{ik}{r_{ij}}\right) \\ b_{ij} = \dfrac{1}{4\pi}\dfrac{e^{ikr_{ij}}}{r_{ij}}\left(-k^2 + \dfrac{3}{r_{ij}^2} - \dfrac{3ik}{r_{ij}}\right) \\ d_{ij} = \dfrac{1}{4\pi}\dfrac{e^{ikr_{ij}}}{r_{ij}}\left(k^2 + \dfrac{ik}{r_{ij}}\right), \end{cases} \tag{5}$$

where r_{ij} denotes the distance between *ith* and *jth* particles and $k = 2\pi/\lambda$. Thus, the total induced electric and magnetic dipoles can be derived as

$$\begin{cases} \vec{p}_i = \alpha_E[\varepsilon_0\vec{E}_0 + \sum_{j\neq i}a_{ij}\vec{p}_j + b_{ij}(\vec{p}_j\cdot\vec{n}_{ji})\vec{n}_{ji} - (d_{ij}/c)(\vec{n}_{ji}\times\vec{m}_j)] \\ \vec{m}_i = \chi_H[\vec{H}_0 + \sum_{j\neq i}a_{ij}\vec{m}_j + b_{ij}(\vec{m}_j\cdot\vec{n}_{ji})\vec{n}_{ji} + d_{ij}c(\vec{n}_{ji}\times\vec{p}_j)], \end{cases} \tag{6}$$

where $c = \sqrt{1/\varepsilon_0\mu_0}$ represents the speed of light in vacuum. For the case of silicon nanoparticles separated by a large distance, the resulting electric and magnetic dipoles can be regarded as equivalent to that of a single nanoparticle since $a_{ij}, b_{ij}, d_{ij} \to 0$ with $r_{ij} \to \infty$. However, in the opposite limit with $r_{ij} \to 0$, the situation changes dramatically. By calculating the scattering spectra, the interactions between silicon nanoparticles can be directly reflected.
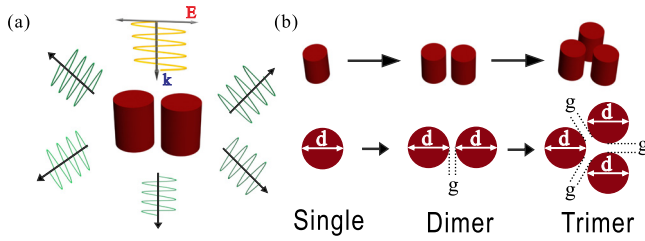
FIG. 1. (a) Schematic view of the scattering process of dimeric silicon nanocylinders. Yellow and green waves represent the incident light and scattered light, respectively. The directions of polarization and wave-vector are marked by gray arrows. (b) Three-dimensional diagrams and cross-section views of single, dimeric, and trimeric nanostructures.

Actually according to Eq. (6), three types of interactions among the induced dipoles may occur in the coupled nanoparticles: the electric-to-electric interaction (i.e., $a_{ij}\vec{p}_j + b_{ij}(\vec{p}_j \cdot \vec{n}_{ji})\vec{n}_{ji}$ in the induced electric dipoles); the electric-to-magnetic interaction (i.e., $-(d_{ij}/c)(\vec{n}_{ji} \times \vec{m}_j)$ in the induced electric dipoles and $d_{ij}c(\vec{n}_{ji} \times \vec{p}_j)$ in the induced magnetic dipoles); and the magnetic-to-magnetic interaction (i.e., $a_{ij}\vec{m}_j + b_{ij}(\vec{m}_j \cdot \vec{n}_{ji})\vec{n}_{ji}$ in the induced magnetic dipoles). By relying on these interactions in the coupled nanoparticles, high-index dielectric antennas are expected to achieve versatile functions, such as broadband optical response. In this work, we theoretically study the scattering properties of dimeric and trimeric silicon nanocylinders. The silicon nanocylinder, as the elementary cell, has a constant diameter $d = 240$ nm and height $h = 240$ nm. The optical constants of silicon are taken from the optical handbook.[34] The resonances of these structures cover the region of visible and near-infrared, which are of great interest in solar-cell applications.[23]

Figure 1(a) shows the schematic of the scattering process when light is incident on a dimer. Dimeric silicon nanocylinders are illuminated by a light source (yellow waves), propagating from top to bottom ($-z$-direction) with polarization along the line of centers in the dimer (x-direction), as indicated by gray arrows. In the following FDTD simulation, we use a commercial software package (Lumerical, FDTD_Solutions version 8.0.1). The plane wave source illuminates the nanostructures, and the simulation region is divided into two parts: the total-field region inside the source and the scattered-field region outside the source. Scattered light (green waves) are collected by a monitor box outside the source and in this manner, the scattering spectra can be obtained. Figure 1(b) shows

three-dimensional diagrams and cross-sectional views (x-y plane) of single, dimeric, and trimeric nanostructures, respectively. The height (h) and diameter (d) of nanocylinder are kept constant at 240 nm, while the gap (g) in the dimeric and trimeric nanostructures can be varied.

III. NUMERICAL RESULTS AND DISCUSSIONS

A. Scattering properties of single silicon nanocylinder

For the purpose of comparison, we first examine the scattering spectrum of a single silicon nanocylinder (orange curve in Fig. 2(a)). Simply, our primary concern is the obvious electric or magnetic resonance, indicated by dashed lines in Fig. 2(a). We note the presence of the two resonant modes reported in many studies:[22–26] a magnetic resonant mode around $\lambda = 1000$ nm and an electric resonant mode around $\lambda = 800$ nm. Instinctively, both resonant modes are diameter-related, and they can be excited at the same optical frequency by changing the aspect ratio of silicon nanocylinders.[25]

To more clearly understand the magnetic and electric resonant modes, we give electric-field intensity ($|E|$) distributions and the magnetic field (H_y) distributions in the x–z plane. Figure 2(b) shows the field distributions of the magnetic mode at $\lambda = 1000$ nm and the electric mode at $\lambda = 800$ nm. From the electric field distribution (left column), we observe that there is a displacement current loop associated with the circulating electric field at $\lambda = 1000$ nm (marked by a white arrow loop) and a linear electric field distribution at $\lambda = 800$ nm (marked by a white arrow). From the magnetic field distribution (right column), we note that the magnetic field distribution indicates the presence of an antinode at the center at $\lambda = 1000$ nm, which is consistent with a magnetic dipole, while at $\lambda = 800$ nm, the distribution indicates the presence of a node at the center, consistent with an electric dipole. All these observations indicate that the resonant mode at $\lambda = 1000$ nm originates from magnetic resonance, while the resonant mode at $\lambda = 800$ nm originates from electric resonance.

B. Broadband scattering of dimeric silicon nanocylinders

In the following section, we study the effect of the interaction of nanocylinders in close proximity on the scattering properties by varying the gap between two nanocylinders. Figure 3(a) shows the scattering spectra of dimeric silicon nanocylinders for various gap sizes ranging from 200 to
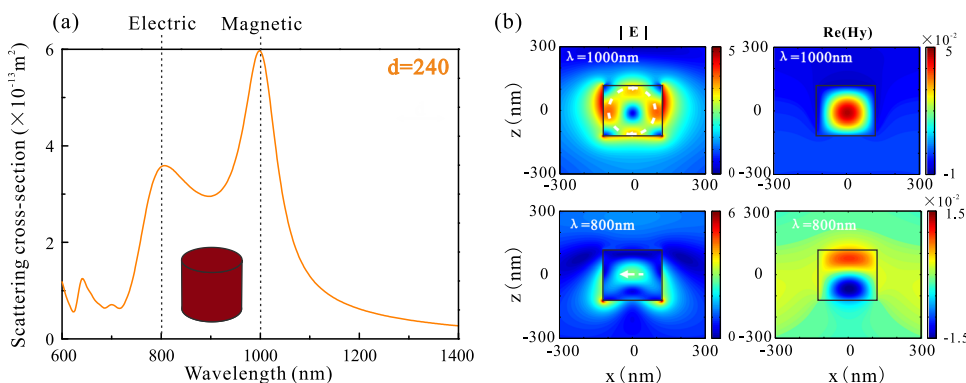

FIG. 2. (a) Calculated scattering cross-section of single silicon nanocylinder. Electric and magnetic resonances are indicated by dashed lines. The inset shows the corresponding nanocylinder configuration. (b) Electric field intensity ($|E|$) distributions and magnetic field (H_y) distributions in the x–z plane of the magnetic resonance at $\lambda = 1000$ nm and electric resonance at $\lambda = 800$ nm. White arrows indicate the direction of electric field.
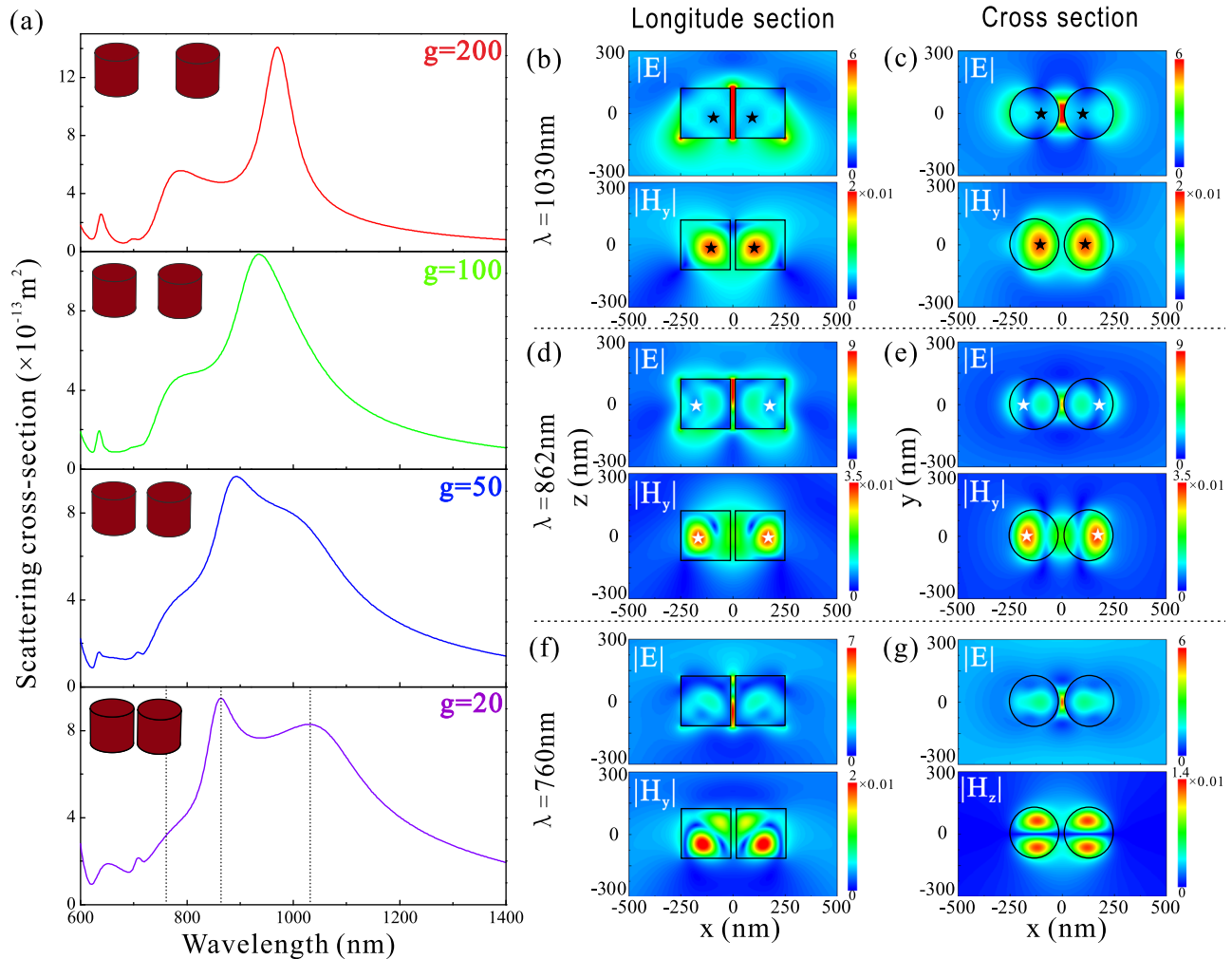
FIG. 3. (a) Calculated scattering spectra of dimers with nanocylinder gaps varying from 200 nm to 20 nm. Both silicon nanocylinders are identical ($d = 240$ nm and $h = 240$ nm). From top to bottom, $g = 200$ nm (red curve), 100 nm (green curve), 50 nm (blue curve), 20 nm (violet curve), respectively. The three spectral positions marked by the three dashed lines in the lowest panel are chosen for field distribution analysis. The insets show the corresponding dimer configuration. (b)–(g) The intensity distributions of electric field ($|E|$) and magnetic field ($|H_y|$) of the dimer with gap $g = 20$ nm at $\lambda = 1030$ nm, 862 nm, and 760 nm, respectively, along the longitudinal section (x–z plane, $y = 0$ nm) and cross-section (x–y plane, $z = 0$ nm). The black and white stars indicate the location of the magnetic dipole corresponding to magnetic resonance at $\lambda = 1030$ nm and $\lambda = 862$ nm, respectively.

20 nm. In the case of a large gap of $g = 200$ nm (red curve), a scattering spectrum similar to that of a single silicon nanocylinder is obtained, corresponding to weak interaction. As the gap decreases, we observe that the electric and magnetic resonances shift closer to each other and the electric resonance becomes less pronounced. When the gap is sufficiently small ($g = 20$ nm), another mode is observed in the longer-wavelength range (violet curve). Different from the electric or magnetic resonance of the single nanocylinder, the newly emergent mode results from the interaction of two nanocylinders in close proximity. Because of the newly emergent mode, dimeric silicon nanocylinders with very small gap exhibit a distinct broadband response, which may be implemented to optical antennas and solar energy applications.

To intuitively understand the newly emergent mode, we study the intensity distributions of electric fields and magnetic fields along the longitudinal and cross-section directions, respectively. Here, we choose the most prominent scattering spectrum of dimeric silicon nanocylinders with the 20 nm gap (violet curve). From the scattering spectrum, we pick out three spectral positions marked by three dashed lines: the newly emergent mode at $\lambda = 1030$ nm, the magnetic resonant mode at $\lambda = 862$ nm and the electric resonant mode at $\lambda = 760$ nm that have shifted from magnetic and electric resonances of the single silicon nanocylinder.

Figures 3(b)–3(g) illustrate the field intensity distributions along the longitudinal and cross-section directions, respectively. From Fig. 3(b), we note that the electric field roughly forms a displacement current loop and the magnetic field shows an antinode in each nanocylinder (indicated by the black stars) locating close to the dimer center at $\lambda = 1030$ nm. In the cross-sectional view in Fig. 3(c), the electric field shows a node and the magnetic field shows an antinode at the center, exhibiting magnetic characteristics consistent with that in Fig. 3(b). Further, the field distributions at $\lambda = 862$ nm (Figs. 3(d) and 3(e)) exhibit similar magnetic resonant properties to those at $\lambda = 1030$ nm; the main difference is that the magnetic field at $\lambda = 862$ nm indicates antinodes located away from the dimer center, as denoted by the white stars. It must be mentioned that at $\lambda = 862$ nm, the

central region of dimer exhibits relatively intense magnetic field showing a contrary direction to that in the silicon nano-cylinder, exhibiting partial electric characteristics. At $\lambda = 760$ nm (Figs. 3(f) and 3(g)), we observe that the electric field exhibits a roughly linear distribution while magnetic field shows a node exhibiting electric characteristics, which is more obvious in the cross-sectional view (Fig. 3(g)). It is noteworthy that the field distributions in dimeric nanocylinders show asymmetric features with respect to those of the single nanocylinder. The electric displacement current loop corresponding to magnetic resonance is no longer equal with opposite direction along the x and z directions and the linear electric distribution corresponding to electric resonance no longer lies simply along the x direction. These changes can be attributed to the introduction of interaction term with different directions in Eq. (6). The resonant modes at $\lambda = 862$ nm and $\lambda = 762$ nm, which are shifted from the magnetic and electric resonances in the single silicon nanocylinder, nearly completely merge with each other and form hybrid resonant modes. Thus, from the abovementioned analysis, we can conclude that as regards the interaction between two silicon nanocylinders in a dimeric nanostructure, the electric and magnetic resonances shift closer to each other, forming hybrid resonant modes; meanwhile, a new magnetic resonant mode attributed to the magnetic-to-magnetic interaction between two silicon nanocylinders in close proximity is observed to emerge.

It is worthwhile to discuss the scattering direction of the abovementioned dimeric silicon nanocylinders. By receiving the scattered light toward the forward or backward direction, respectively, we have obtained the forward (black curve) and the backward (blue curve) scattering spectra of the four dimeric silicon nanocylinders together with the forward-to-backward ratio (orange curve), as shown in Fig. 4. It is obvious that the dimer with weak interaction ($g = 200$ nm) exhibits highly directional scattering within a narrow spectral region. As the gap decreases in the dimer, the interaction between nanocylinders becomes stronger thus the forward-to-backward ratio keeps a high value within a broader band. This feature may contribute to the design of broadband directional dielectric antennas.[35–37]

Next, we attempt to provide more evidence to demonstrate the newly emergent magnetic resonant mode. Here, we consider two periodic arrays: a dimeric nanocylinders array with weak coupling (diameter: $d = 240$ nm; gap: $g = 200$ nm;

periodicities of lattice: $a_x = 880$ nm and $a_y = 440$ nm; spacing between adjacent units: $d_x = 200$ nm and $d_y = 200$ nm) and a dimeric nanocylinders array with strong coupling (diameter: $d = 240$ nm; gap: $g = 20$ nm; periodicities of lattice: $a_x = 880$ nm and $a_y = 440$ nm; spacing between adjacent units: $d_x = 380$ nm and $d_y = 200$ nm). The left parts in Figs. 5(a) and 5(d) show the schematic arrangements. Please note that the former has $g = 200$ nm and $d_x = d_y = 200$ nm (Fig. 5(a)), thus the system can simply be regarded as a single nanocylinder array with weak interaction, in which adjacent silicon nanocylinders are separated by the 200 nm-wide gaps. When decreasing the gap to $g = 20$ nm in each unit and enlarging d_x to be 380 nm (Fig. 5(d)), the system can be regarded obviously as a dimeric nanocylinders array with strong coupling.

We consider the whole structure effectively as a homogeneous slab with the thickness equal to the height of silicon nanocylinders, and derive the effective permittivity and permeability from the normal reflection and transmission coefficients, analyzed by a robust retrieval algorithm.[38] Figures 5(a) and 5(d) show the transmission spectra of the two arrays which exhibit resonant characteristics similar to their corresponding scattering spectra, while Figs. 5(b) and 5(c) and Figs. 5(e) and 5(f) show the corresponding effective permittivity and permeability. There is an obvious negative electric response around $\lambda = 780$ nm, as shown in Fig. 5(b). In addition, a magnetic anti-resonance response accompanies the electric response. Evidently, there is a drop of Re(μ) and negative values of Im(μ) in Fig. 5(c). During the resonance, the electric field is attenuated with positive Im(ε) and magnetic field is gained with negative Im(μ). Thus, the system obeys the conservation of energy. For the resonance around $\lambda = 930$ nm, there is an obvious negative magnetic response (Fig. 5(c)) accompanied by an electric anti-resonance response (a drop of Re(ε) and negative values of Im(ε) in Fig. 5(b)) which can be analog to the above magnetic anti-resonance. These properties confirm electric resonance in the shorter-wavelength range and magnetic resonance in the longer-wavelength range in the single nanocylinder. Similarly, for the dimer array with strong coupling, we can evidently recognize the newly emergent mode around $\lambda = 1080$ nm as magnetic resonance, exhibiting an obvious negative magnetic response (Fig. 5(f)). While the mode around $\lambda = 860$ nm is difficult to resolve into electric or magnetic resonance from the effective permittivity and
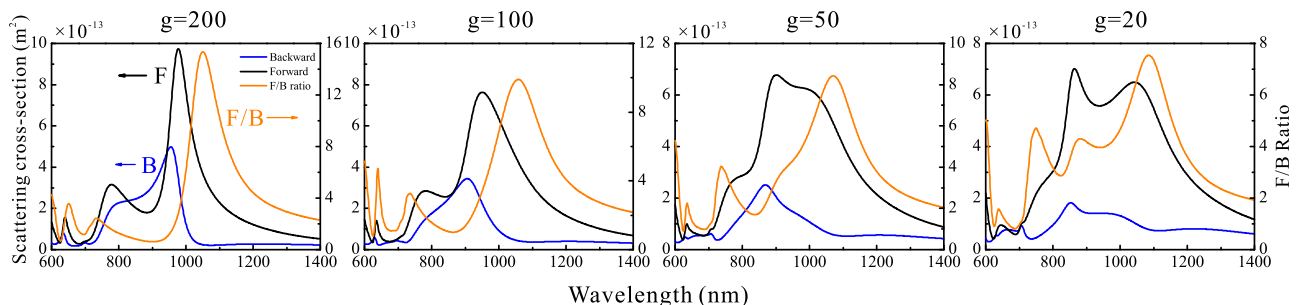

FIG. 4. The calculated forward (black curve) and backward (blue curve) scattering spectra of dimers with nanocylinder gaps varying from 200 nm to 20 nm together with the forward-to-backward ratio (orange curve). From left to right, $g = 200$ nm, 100 nm, 50 nm, 20 nm, respectively.
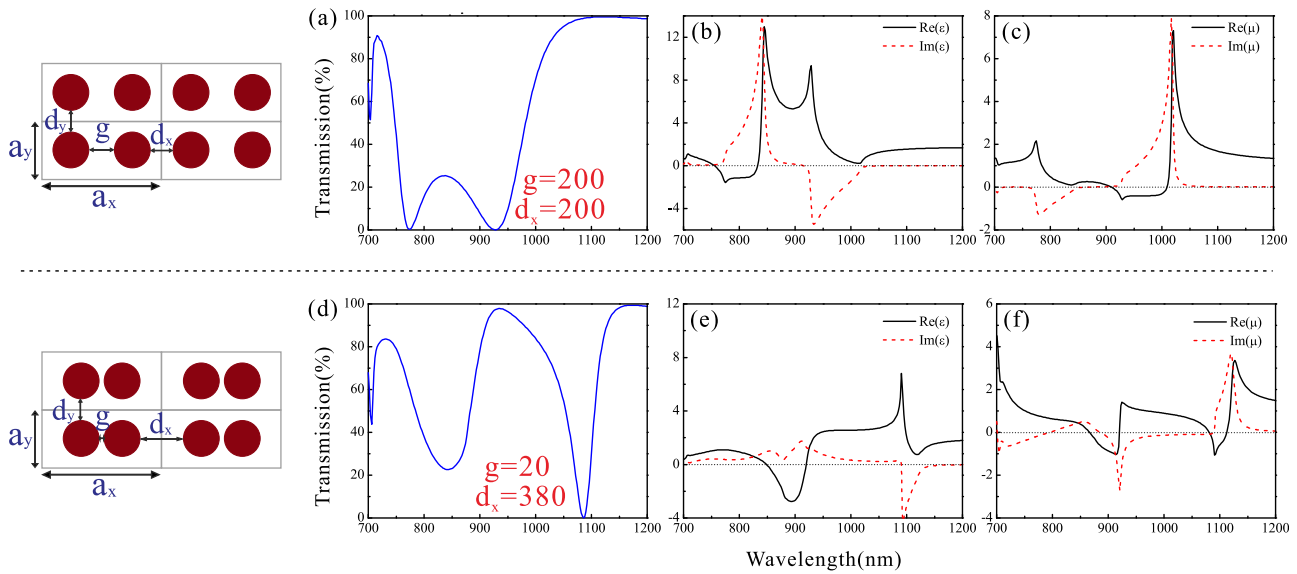
FIG. 5. Calculated normal transmission spectra for (a) the dimeric silicon nanocylinder array with weak coupling and (d) the dimeric silicon nanocylinder array with strong coupling in air medium. The left shows the array configuration. The periodicities of the lattice are $a_x = 880$ nm and $a_y = 440$ nm. The variable parameters $g = 200$ nm, $d_x = 200$ nm for (a) and $g = 20$ nm, $d_x = 380$ nm for (d). (b) and (c) Retrieved permittivity ε and permeability μ for the dimeric silicon nanocylinder array with weak coupling. (e) and (f) Retrieved permittivity ε and permeability μ for the dimeric silicon nanocylinder array with strong coupling. The black solid and red dashed curves indicate the real and imaginary parts, respectively.

permeability because the electric and magnetic resonances merge with each other and turn out to form hybridized resonant modes.

C. Broadband scattering of trimeric silicon nanocylinders

Similar to the abovementioned dimeric nanostructure, we can also construct trimeric silicon nanocylinders which introduce an even more complex interaction. In the manner of the dimeric nanostructure, more intense broadband response can also be obtained promisingly.

Figure 6(a) shows the scattering spectra of trimeric silicon nanocylinders with the gap $g = 20$ nm (top panel, green curve) and $g = 60$ nm (bottom panel, red curve). In the case of gap $g = 20$ nm (green curve), which corresponds to intense interaction, an evident magnetic resonance splitting emerges and the newly emergent magnetic mode becomes more pronounced than that in the dimeric nanostructure. However,

well-separated resonant modes due to intense interaction lead to a prominent dip around $\lambda = 1000$ nm, which can be disadvantageous in broadband applications. To overcome this disadvantage, a continuous broadband response can be obtained by appropriately adjusting the trimeric gap to 60 nm (red curve), thereby partly sacrificing the bandwidth of newly emergent pronounced magnetic mode. In this manner, synthetical effect containing both broadband and continuity requirements can be satisfied.

Referring to the full width at half maximum (FWHM), we use the bandwidth span of the half maxima scattering peak to characterize the response bandwidth. Figure 6(b) shows the bandwidth column diagram of the single (orange column), dimer with gap $g = 20$ nm (violet column), and trimer with gap $g = 20$ nm (green column) and $g = 60$ nm (red column), respectively. In comparison with the single, the bandwidth increases by 30% for the dimer with gap $g = 20$ nm (violet column) and by 50% in the trimer with gap $g = 60$ nm (red column). Ignoring the prominent dip for the trimer with gap
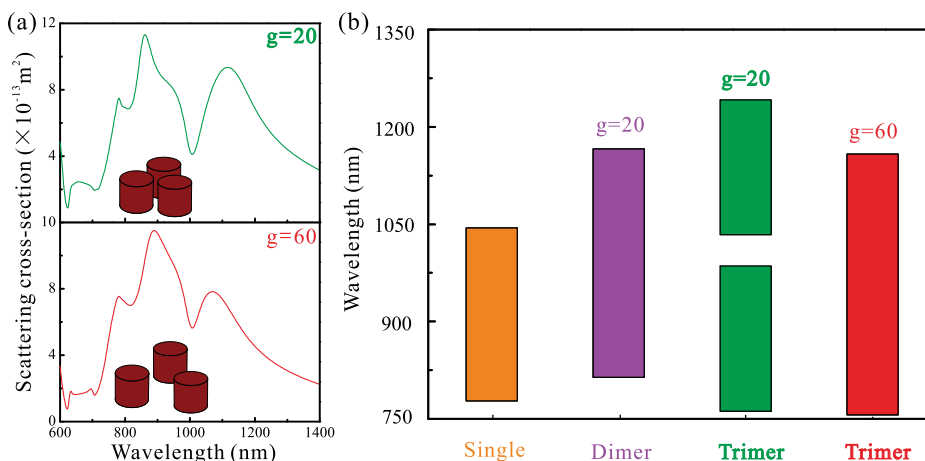

FIG. 6. (a) Calculated scattering spectra of trimers with gap $g = 20$ nm (top panel, green curve) and $g = 60$ nm (bottom panel, red curve). The insets show the corresponding trimer configuration. (b) Summarized bandwidth column diagram of single nanocylinder (orange column), dimer with gap $g = 20$ nm (violet column), and trimer with gap $g = 20$ nm (green column) and $g = 60$ nm (red column).

$g = 20$ nm (green column), the increase can even reach 60%. Such broadband scattering responses indicate enormous potential for solar cells and silicon-based nano devices.

IV. CONCLUSIONS

In the light of resonances in the single silicon nanocylinder, we have theoretically demonstrated the broadband scattering properties of dimeric and trimeric silicon nanocylinders. As the dimer gap decreases, the magnetic and electric resonances of the constituent single nanocylinders shift close to each other, forming hybrid modes. At the same time, a new magnetic resonance mode emerges in the longer-wavelength region which can be attributed to the intense magnetic-to-magnetic interaction between the two nanocylinders. Both the field distributions and the effective permittivity and permeability confirm the magnetic resonant characteristic at optical frequencies. Further bandwidth increase can be obtained using trimeric silicon nanocylinders for introducing more intense interaction. Referring to the FWHM, we use the bandwidth span of the half maxima scattering peak to characterize the response bandwidth. In comparison with the single silicon nanocylinder, the dimer and trimer exhibit evident continuous bandwidth increase. The continuous bandwidth increase can reach 50% by adjusting the gap in the trimeric silicon nanocylinders configuration. Our theoretical findings can potentially be useful in constructing dielectric nanoantennas and nanodetectors, and in broadband applications such as solar cells.

ACKNOWLEDGMENTS

[1]L. Novotny and B. Hecht, *Principles of Nano-Optics* (Cambridge University Press, Cambridge, 2006).

[2]A. V. Zayats, I. I. Smolyaninov, and A. A. Maradudin, Phys. Rep. **408**, 131 (2005).

[3]L. Novotny and N. van Hulst, Nat. Photonics **5**, 83 (2011).

[4]Z. J. Zhang, R. W. Peng, Z. Wang, F. Gao, X. R. Huang, W. H. Sun, Q. J. Wang, and M. Wang, Appl. Phys. Lett. **93**, 171110 (2008).

[5]F. J. González and G. D. Boreman, Infrared Phys. Technol. **46**, 418 (2005).

[6]A. G. Curto, G. Volpe, T. H. Taminiau, M. P. Kreuzer, R. Quidant, and N. F. van Hulst, Science **329**, 930 (2010).

[7]T. Kosako, Y. Kadoya, and H. F. Hofmann, Nat. Photonics **4**, 312 (2010).

[8]P. Biagioni, J. S. Huang, L. Duò, M. Finazzi, and B. Hecht, Phys. Rev. Lett. **102**, 256801 (2009).

[9]Q. Zhao, J. Zhou, F. Zhang, and D. Lippens, Mater. Today **12**, 60 (2009).

[10]C. M. Soukoulis and M. Wegener, Nat. Photonics **5**, 523 (2011).

[11]D. S. Filonov, A. E. Krasnov, A. P. Slobozhanyuk, P. V. Kapitanova, E. A. Nenasheva, Y. S. Kivshar, and P. A. Belov, Appl. Phys. Lett. **100**, 201113 (2012).

[12]A. E. Krasnok, A. E. Miroshnichenko, P. A. Belov, and Y. S. Kivshar, Opt. Express **20**, 20599 (2012).

[13]L. Zou, W. Withayachumnankul, C. M. Shah, A. Mitchell, M. Bhaskaran, S. Sriram, and C. Fumeaux, Opt. Express **21**, 1344 (2013).

[14]A. E. Miroshnichenko, B. Luk'yanchuk, S. A. Maier, and Y. S. Kivshar, ACS Nano **6**, 837 (2012).

[15]A. García-Etxarri, R. Gómez-Medina, L. S. Froufe-Pérez, C. López, L. Chantada, F. Scheffold, J. Aizpurua, M. Nieto-Vesperinas, and J. J. Sáenz, Opt. Express **19**, 4815 (2011).

[16]J. C. Ginn, I. Brener, D. W. Peters, J. R. Wendt, J. O. Stevens, P. F. Hines, L. I. Basilio, L. K. Warne, J. F. Ihlefeld, P. G. Clem, and M. B. Sinclair, Phys. Rev. Lett. **108**, 097402 (2012).

[17]Y. H. Fu, A. I. Kuznetsov, A. E. Miroshnichenko, Y. F. Yu, and B. Luk'yanchuk, Nat. Commun. **4**, 1527 (2013).

[18]A. I. Kuznetsov, A. E. Miroshnichenko, Y. H. Fu, J. B. Zhang, and B. Luk'yanchuk, Sci. Rep. **2**, 492 (2012).

[19]A. B. Evlyukhin, S. M. Novikov, U. Zywietz, R. L. Eriksen, C. Reinhardt, S. I. Bozhevolnyi, and B. N. Chichkov, Nano Lett. **12**, 3749 (2012).

[20]C. Enkrich, M. Wegener, S. Linden, S. Burger, L. Zschiedrich, F. Schmidt, J. F. Zhou, Th. Koschny, and C. M. Soukoulis, Phys. Rev. Lett. **95**, 203901 (2005).

[21]D. Li, L. Qin, X. Xiong, R. W. Peng, Q. Hu, G. B. Ma, H. S. Zhou, and M. Wang, Opt. Express **19**, 22942 (2011).

[22]A. B. Evlyukhin, R. L. Eriksen, W. Cheng, J. Beermann, C. Reinhardt, A. Petrov, S. Prorok, M. Eich, B. N. Chichkov, and S. I. Bozhevolnyi, Sci. Rep. **4**, 4126 (2014).ôôôô

[23]N. T. Fofang, T. S. Luk, M. Okandan, G. N. Nielson, and I. Brener, Opt. Express **21**, 4774 (2013).

[24]J. van de Groep and A. Polman, Opt. Express **21**, 26285 (2013).

[25]I. Staude, A. E. Miroshnichenko, M. Decker, N. T. Fofang, S. Liu, E. Gonzales, J. Dominguez, T. S. Luk, D. N. Neshev, I. Brener, and Y. Kivshar, ACS Nano **7**, 7824 (2013).

[26]F. J. Bezares, J. P. Long, O. J. Glembocki, J. Guo, R. W. Rendell, R. Kasica, L. Shirey, J. C. Owrutsky, and J. D. Caldwell, Opt. Express **21**, 27587 (2013).

[27]A. E. Miroshnichenko and Y. S. Kivshar, Nano Lett. **12**, 6459 (2012).

[28]D. S. Filonov, A. P. Slobozhanyuk, A. E. Krasnok, P. A. Belov, E. A. Nenasheva, B. Hopkins, A. E. Miroshnichenko, and Y. S. Kivshar, Appl. Phys. Lett. **104**, 021104 (2014).

[29]G. Boudarham, R. Abdeddaim, and N. Bonod, Appl. Phys. Lett. **104**, 021117 (2014).

[30]P. Albella, M. A. Poyli, M. K. Schmidt, S. A. Maier, F. Moreno, J. J. Sáenz, and J. Aizpurua, J. Phys. Chem. C **117**, 13573 (2013).

[31]B. Rolly, B. Bebey, S. Bidault, B. Stout, and N. Bonod, Phys. Rev. B **85**, 245432 (2012).

[32]A. Taflove and S. C. Hagness, *Computational Electrodynamics: The Finite-Difference Time-Domain Method* (Artech House, Norwood, 2000).

[33]G. W. Mulholland, C. F. Bohren, and K. A. Fuller, Langmuir **10**, 2533 (1994).

[34]E. D. Palik, *Handbook of Optical Constants of Solids* (Academic, New York, 1985), Vol. 1, p. 555.

[35]A. E. Krasnok, D. S. Filonov, C. R. Simovski, Y. S. Kivshar, and P. A. Belov, Appl. Phys. Lett. **104**, 133502 (2014).

[36]B. Rolly, B. Stout, and N. Bonod, Opt. Express **20**, 20376 (2012).

[37]B. Rolly, J.-M. Geffrin, R. Abdeddaim, B. Stout, and N. Bonod, Sci. Rep. **3**, 3063 (2013).ôôôô

[38]D. R. Smith, S. Schultz, P. Markoš, and C. M. Soukoulis, Phys. Rev. B **65**, 195104 (2002).